Northumbria Research Link

Flexible and Bendable Acoustofluidics for Particle and Cell Patterning

Sadaf Maramizonouz,[1,*] Xiang Tao,[2,*] Mohammad Rahmati,[1,♠] Changfeng Jia,[4] Ran Tao,[1,3] Hamdi Torun,[1] Tengfei Zheng,[4] Hao Jin,[2] Shurong Dong,[2] Jikui Luo,[2] Yongqing Fu[1,♣]

[1] Faculty of Engineering and Environment, Northumbria University, Newcastle upon Tyne, NE1 8ST, UK

[2] College of Information Science and Electronic Engineering, Zhejiang University, Hangzhou 310027, China

[3] Shenzhen Key Laboratory of Advanced Thin Films and Applications, College of Physics and Optoelectronic Engineering, Shenzhen University, Shenzhen, 518060, China

[4] State Key Laboratory for Manufacturing Systems Engineering, Xi'an Jiaotong University, Xi'an, 710049, China

Abstract: Surface acoustic wave (SAW) based microfluidic devices provide active techniques to manipulate fluid and particles, which can be used for precise and controllable patterning of microparticles and biological cells, with a high efficiency in a non-invasive and contact-free manner. This paper investigates flexible and bendable SAW microfluidic devices and explores the effects of bending and twisting of SAW devices on microparticle and cell patterning, using both experimental and numerical modelling. We showed that bending flexible SAW devices changes the distribution of particle pattern lines significantly. In devices with concave bending the particle pattern lines converge towards the centre of the curvature, whereas for devices with convex bending, they diverge away from it. Comparing the particle patterning using Lamb and Rayleigh wave devices with concave bending, we found that particle alignment is more efficient in the flexural mode Lamb wave device, whereas for the devices with convex bending, the particle patterning is more clear and regular when Rayleigh waves are used. We further investigated the effects of twisting the flexible SAW devices and observed that the particles are patterned into lines parallel to the deformed interdigital transducers (IDTs). We finally patterned yeast cells using our flexible SAW devices, and demonstrated the possibility of using our flexible acoustofluidic device for biomechanical systems such as body conforming technologies, wearable bio-sensors, and flexible point-of-care devices for personalized health monitoring.

Keywords: Flexible Acoustofluidics, Particle and Cell Patterning, Thin Film SAW Devices

1 Introduction

Applications of ultrasonics and surface acoustic waves (SAWs) in microfluidic platforms (often called acoustofluidics) have gained great interest for manipulating fluids, microparticles and cells, in either a digital format (sessile droplet) or continuous flow (inside a microchannel/chamber) [1-3]. These acoustofluidic devices offer great potentials in the fields of biomechanics, medicine and chemistry [4-7] for non-invasive and contact-free manipulation, with good biocompatibility, conserved cell viability and proliferation capacity [8-12]. Acoustic tweezers fabricated using the SAW devices can be used for manipulating, patterning and controlling microparticles and biological cells with a high precision [13-17].

---

[*] These authors have equal contribution to this paper.

[♠] Corresponding Author: Dr. Mohammad Rahmati, E-mail: mohammad.rahmati@northumbria.ac.uk

[♣] Corresponding Author: Prof. Richard Yongqing Fu, E-mail: richard.fu@northumbria.ac.uk

For the conventional acoustofluidic platforms, standing surface acoustic waves (SSAWs) can be readily generated between the two electrodes of the SAW devices when a radio frequency (RF) signal is applied to the electrodes. The acoustic field generated by the propagation of the SAWs forces the particles to form parallel lines along the width of the microchamber with a constant distance between each two adjacent lines corresponding to the pressure node lines (with minimum acoustic pressure) of the standing acoustic waves (shown in Figure 1(a)). This alignment can be clearly observed from the top view, which has been well documented in literature [13, 14, 17]. Particle distribution and alignment along the height of the microchamber have also recently been investigated and it was demonstrated that particles form pattern lines in a three-dimensional matrix [15, 16].

Flexible microfluidic platforms could be used for on-body applications, wearable devices, body conforming technologies, implantable biomedical applications , flexible sensors or soft robotics, to monitor physiological conditions of a patient, detect infection illness or even cancer at its early stages [18-20]. They have recently shown promises in constructing medical and bio-inspired devices [21], micro-stretching devices for cell studies [22], cell sorting bandages, wearable [23] and point-of-care (POC) devices [24] for monitoring the body temperature, heart rate or blood pressure, clinical and biomedical technologies for collection, manipulation and investigation of bodily fluids [25, 26] such as detecting antigen and antibody reactions [27], deep brain stimulation [28], artificial retina [28] and wearable devices for flow measurement in a cerebrospinal shunt [29].

Recently, there are studies to design and fabricate flexible (including bendable, deformable and even stretchable) ultrasonic and SAW devices [30-32]. For example, flexible SAW sensors and acoustofluidics devices were fabricated by depositing a thin layer of a piezoelectric material such as zinc oxide (ZnO) or aluminium nitride (AlN) onto a flexible substrate (either polymer or metallic foil such as aluminium), followed by patterning of interdigital transducers (IDTs) on top of the piezoelectric thin film [6, 33-36]. Our results showed that the SAW devices based on ZnO on aluminium (Al) foil/sheet demonstrate efficient acoustofluidic functions to drive liquid sessile droplets on both flat, inclined and even randomly bent and curved surfaces [33, 36].

It is crucial to understand the dynamic behaviour and 3D distribution patterns of the particles and biological cells under acoustic waves in a potentially bendable acoustofluidic device. However, so far, there are no previous studies on flexible and deformable SAW devices used in continuous-flow acoustofluidic platforms for patterning of microparticles and biological cells. This study aims to understand the acoustofluidic behaviour when the SAW devices are in different bent conditions, and the effects of bending curvatures on microparticle manipulation and patterning of particles and cells inside a microchamber or a microchannel under the SSAWs.

A flexible SAW device can be bent in both concave (see Figures 1(b)) and convex (see Figures 1(c)) geometries. Accordingly, all the particles or cells could still be aligned in parallel by the SSAWs along the IDT direction. However, from the cross-sectional views along the vertical direction, the patterned lines of particle will not have a constant distance from the bottom of chamber to the top, and particle pattern lines might become converged with a slope towards the centre of the curvature of the geometry from the cross-sectional view. From the top views, the distances between each two adjacent parallel lines (we will use "line distance" in short hereafter) of the particles or cells can be varied. In this paper, we will numerically and experimentally study the flexible and bendable devices in both concave (substrate bent-down, (Figure 1(b)) and convex (substrate bent-up, Figure 1(c)) geometries. We then further studied

a twisting configuration (Figure 1(d)) using ZnO thin film SAW devices made on aluminium foil/sheets, and we will investigate the microparticles' patterning with the changes of directions of the twisted IDTs for different twisting geometries.
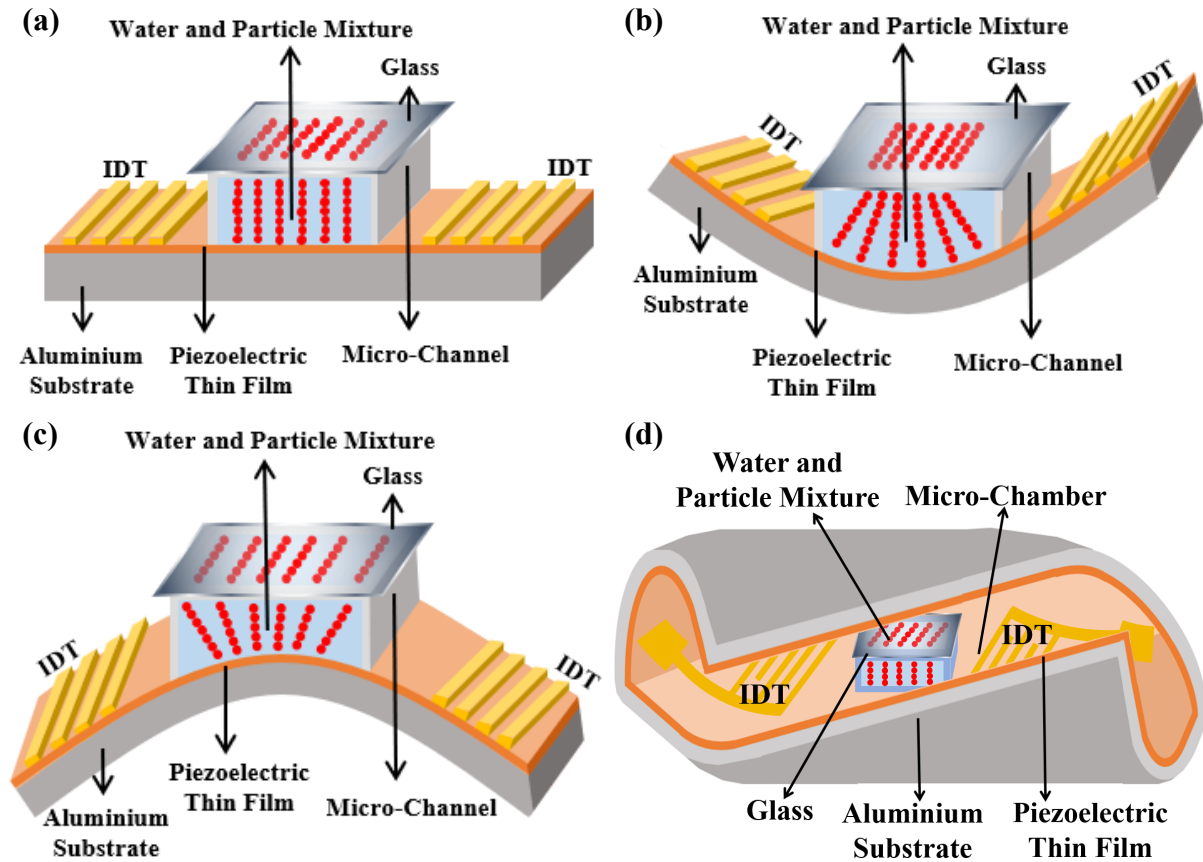

Figure 1 Schematic of the effect of bending the flexible SAW device on particle patterning in a microchamber with (a) flat, (b) concave (bent-down), (c) convex (bent-up) and (d) twisting surfaces.

2   Experimental Details

We designed different experiments to investigate the key factors to influence the 3D patterning of particles in the bent flexible devices. All the flexible SAW devices were fabricated by depositing ~5 μm thick ZnO film onto two types of aluminium substrates (Al foils with a thickness of 50 μm and Al sheets with a thickness of 200 μm) using a direct current (DC) magnetron sputter (NS3750, Nordiko). During the deposition process, the substrates were rotated without any intentional substrate heating. Zinc target with 99.99% purity was used in the sputtering process, and the deposition parameters are: Ar/O_2 flow ratio of 10/15, vacuum chamber pressure of ~0.35 Pa and power of 400 Watts [6, 37]. The deposited ZnO film has a strong texture of (0002) crystal orientation. Aluminium was chosen as the substrate because it is flexible and can be bent and twisted to form the desired shapes with minimal force and it has a low sound absorption coefficient so it does not absorb/dampen the wave.

The IDTs (made from 20/100 nm thick of Cr/Au) of the SAW devices were fabricated using a standard photolithography and lift-off process. The designed IDTs had 30 pairs of fingers with an aperture of 49 mm and two different wavelengths (160 μm and 400 μm). An RF network analyser (Keysight, FieldFox N9913A) was used to measure the reflection spectra (S11 parameter) of the SAW devices. Three types of flexible SAW devices (with different substrate thicknesses and wavelengths) were used in the experiments of microparticle patterning in a microchamber. Table 1 lists the detailed information for all the flexible SAW devices

(Figure S-1 in the supplementary information shows the obtained frequency S11 results and the simulated vibration modes for the above three devices).

Table 1 Substrate thickness, wavelengths and resonance frequencies of the flexible SAW devices. Devices 1 and 2 have Lamb wave modes, and Device 3 has Rayleigh wave mode.

Device Name	Al substrate thickness (μm)	Wavelength (μm)	R0 Frequency (MHz)	A0 Frequency (MHz)	S0 Frequency (MHz)	A1 Frequency (MHz)	S1 Frequency (MHz)
Device 1	~50	160	-	13.00	29.06	40.00	47.00
Device 2	200	400	-	6.03	10.83	14.77	16.43
Device 3	200	160	17.00	-	-	-	-

To visualise particle patterning under the effect of SSAWs, a rectangular polydimethylsiloxane (PDMS) microchamber (Sylgard 184 Silicone Elastomer; Dow Corning, USA) with dimensions of 1000 μm × 700 μm × 1000 μm (W × H × L) was temporary bonded onto the bent SAW device surface using a small amount of liquid PDMS at the bottom of PDMS chamber and was pressed tightly onto the sample surface between a pair of identical IDTs. The microchamber was then filled with microparticle/cell suspension in deionised (DI) water and was covered with a piece of glass (with a thickness of 50 μm). Particle patterning was visualized using both silica (with a diameter of 5 μm and a density of 1900 kg/m^3) and polystyrene (with a diameter of 10 μm and a density of 1500 kg/m^3). Yeast cells were also used for demonstration of biological applications since yeast cells can be used as model organisms in cellular biological studies as they can be managed easily during experimental work [38]. The ability to manipulate yeast as model cells in an acoustofluidic setup has a significant potential for biological and biomedical applications such as tissue engineering and microarrays [7, 16].

An RF signal generator (Marconi Instruments 2024) was connected to an amplifier (Amplifier Research 75A) in order to generate the amplified RF signals of the resonant frequencies to the IDT of the SAW devices. The SAW device was placed over a large aluminium bulk holder to minimize the heating effect. A video camera (Imaging Source, DFK 22BUC03) was used to capture the motion of the fluid and the microparticles. The open source image processing software "ImageJ" was used for post-processing the experimental images and to measure the line distances.

3   Theoretical Analysis and Simulation Details

The fundamental physics of this study is mainly based on the behaviours and motions of microparticles and biological cells dispersed in water and inside an standing acoustic wave field. Here, we performed the modelling of the dispersed microparticle phase by individually tracking a large number of particles using the Euler-Lagrange approach. Using this approach, the detailed information of position and velocity for each particle can be obtained. The governing equations of motion for a single particle using the Euler-Lagrange approach are as follows [39, 40]:

$$\frac{\partial \boldsymbol{X}_p}{\partial t} = \boldsymbol{U}_p \tag{1}$$

$$\frac{\partial \rho_p \boldsymbol{U}_p}{\partial t} = \rho_p \frac{\boldsymbol{U}_f - \boldsymbol{U}_p}{\tau_p} + \boldsymbol{W} + \boldsymbol{F}_{AR} \tag{2}$$

where X_p is the particle position vector, t is time, U_p is the particle velocity vector, ρ_p is the particle density, U_f is the fluid velocity vector, $\tau_p = \rho_p d^2/18\mu_f$ is the particle characteristic time, d is the particle diameter, μ_f is the fluid viscosity, $W = (\rho_p - \rho_f)g$ is the gravity and buoyancy force, ρ_f is the fluid density and F_{AR} is the acoustic force acting on the particle. The first term in the right-hand side of Equation (2) is the viscous drag force that the particles experience when they are moving through the fluid. This drag force depends on the properties of the fluid, the properties of the particles and the velocity of the particle relative to the flow and is given by the Stokes's drag law [13, 39]:

$$D = 6\pi\mu_f r U_{relative} \qquad (3)$$

where $U_{relative} = U_f - U_p$ is the fluid velocity relative to the particle velocity [13, 39]. It should be noted that the term $\frac{U_f - U_p}{\tau_p}$ in Equation (2) represents the Stokes drag force on the particles' unit volume.

When two identical SAWs propagate in the opposite directions, their superposition leads to constructive or destructive interference, thus resulting in a standing surface acoustic wave (SSAW) [5]. As the SSAW comes across a fluid in a microchamber, the acoustic energy refracts into the fluid and affects the particles suspended in it. Thus each particle suspended in the fluid is subjected to acoustic forces from both directions. For a spherical particle suspended in a fluid medium in a standing acoustic wave field the acoustic radiation force (ARF), F_{AR}, is described as follows [41-46]:

$$F_{AR} = \frac{-4\pi}{3}r^3 \left[f_1(\tilde{\beta})\beta_f \langle P_{in}\nabla P_{in}\rangle - f_2(\tilde{\rho})\rho_f \frac{3}{2}\langle (V_{in} \cdot \nabla)V_{in}\rangle \right] \qquad (4)$$

$$f_1(\tilde{\beta}) = 1 - \tilde{\beta} \qquad with \qquad \tilde{\beta} = \frac{\beta_p}{\beta_f} \qquad (5)$$

$$f_2(\tilde{\rho}) = \frac{2(\tilde{\rho} - 1)}{2\tilde{\rho} + 1} \qquad with \qquad \tilde{\rho} = \frac{\rho_p}{\rho_f} \qquad (6)$$

where r is the particle radius, β_f is the fluid compressibility, P_{in} and V_{in} are the acoustic pressure and velocity fields and β_p is the particle compressibility. For a one-dimensional SSAW, Equation (4) can be simplified as follows [41-46]:

$$F_{AR_x} = 2\pi r^3 E_{ac} k \sin(2kx) \phi(\tilde{\beta}, \tilde{\rho}) \qquad (7)$$

where $E_{ac} = \frac{1}{2}\beta_f P_{ac}^2$ is the acoustic energy density of the wave, $k = \frac{2\pi}{\lambda}$ is the wavenumber and x is the particle's distance from the nearest pressure node (or anti-node) along the wave propagation direction [41-46]. $\phi(\tilde{\beta}, \tilde{\rho})$ is called the acoustic contrast factor and is defined using the following equation [41-47]:

$$\phi(\tilde{\beta}, \tilde{\rho}) = \frac{1}{3}f_1(\tilde{\beta}) + \frac{1}{2}f_2(\tilde{\rho}) \qquad (8)$$

The acoustic radiation force due to SSAWs can direct each particle towards either the pressure node (minimum pressure amplitude) or the pressure antinode (maximum pressure amplitude) depending on the physical and mechanical properties of objects in the chamber. The acoustic contrast factor's sign defines each particle moves whether towards the pressure node ($\phi(\tilde{\beta}, \tilde{\rho}) > 0$) or towards the pressure antinode ($\phi(\tilde{\beta}, \tilde{\rho}) < 0$) under the effect of acoustic

radiation force [41-47]. As solid objects of silica microparticles, polystyrene microparticles or yeast cells suspended in water were used in this study ($\emptyset(\tilde{\beta}, \tilde{\rho}) > 0$), they were driven to the pressure nodes. It can be seen from the Equation (7) that the ARF has a sinusoidal distribution with a period of half of the wavelength. This results in the distance between particle pattern lines to be theoretically equal to half of the wavelength of the SSAW for a flat conventional SAW device.

For particles with a size lager than a size limit, the effects of acoustic radiation force on the particles are significant. Whereas the particles with a size smaller than the size limit will follow the fluid streamlines [5, 13]. It was shown that this "size limit" depends on variables such as frequency, density, compressibility and viscosity [5, 48].

Based on the above equations, numerical simulations were performed using the commercial software package COMSOL Multiphysics (5.3). The geometry was modelled as a two-dimensional cross-sectional view of the microchamber on the SAW device and was discretized using 5500 structured quadrilateral elements (Figure S-2 in the supplementary information shows the modelled geometry and mesh for one of the SAW device geometries).

To model the acoustic field induced by the SSAW, the Helmholtz equation was solved with impedance boundary conditions on the two sides and the upper wall. The velocity of the surface wave propagating on the ZnO piezoelectric substrate was defined on the lower wall as follows [49]:

$$u_{x-wall} = A_y \zeta \omega \left[e^{-Cd(0.5W-x)} e^{i[-k(0.5W-x)]} + e^{-Cd(0.5W+x)} e^{i[k(0.5W-x)]} \right] \qquad (9)$$

$$u_{y-wall} = A_y \omega \left[e^{-Cd(0.5W-x)} e^{i[-k(0.5W-x)-\pi/2]} - e^{-Cd(0.5W+x)} e^{i[k(0.5W-x)-\pi/2]} \right] \qquad (10)$$

where u_{x-wall} and u_{y-wall} are the surface wave velocities in the x and y directions, respectively, A_y is the wave's displacement amplitude, ω is the wave's angular frequency, Cd is the wave attenuation coefficient, w is the channel width, k is the wave number, x is the longitudinal direction and $\zeta = A_x / A_y$ is the ratio of the displacement amplitudes in x and y directions [49]. The finite element method (FEM) and the multifrontal massively parallel sparse (MUMPS) were used to discretize and solve the governing equations [50].

For modelling the microparticles' behaviour, the differential equations that govern the particle motion (Equations (1) and (2)) were solved for each particle using the generalized minimal residual (GMRES) iterative in two dimensions. At each time step, the acoustic radiation (Equation (7)) and drag (Equation (3)) forces affecting the particle movement were calculated based on the acoustic and fluid field variables. Finally, the particles' positions were continuously tracked and this process was repeated until it reached the specified end time of the simulation. As the volume fraction of the microparticle phase (dispersed phase) is smaller than the volume fraction of the water phase (continuous phase), we can assume that the fluid particle mixture is sparsely distributed. The sizes of the microparticles are insignificant compared to the microchamber dimensions and the velocities of the microparticles are low. Thus, we can assume a "one-way coupling" occurs between the two phases (fluid and particle), which means that the continuous phase affects the dispersed phase but not vice-versa [50].

4   Results and Discussions

4.1   Lamb Wave Based SSAW on Al Foil with 160 μm Wavelength

Firstly, effects of bending curvatures of ZnO on Al foil flexible Device 1 (with a substrate thickness of ~ 50 μm and a wavelength of 160 μm and its details are given in Table 1) on patterning of silica microparticle in a microchamber were studied. In this case, the Lamb wave modes are the dominant frequency modes (see the supplementary information).

The curvature formula ($K(x)$) for any curve with the equation $y = y(x)$ in cartesian coordinates can be calculated as follows:

$$K(x) = \frac{y''}{(1 + y'^2)^{3/2}} \tag{11}$$

where $y'' = \frac{d^2 y}{d^2 x}$ is the second order derivative and $y' = \frac{dy}{dx}$ is the first order derivative of the curve equation $y = y(x)$ in cartesian coordinates. The value of the curvature (K) for the concave and convex SAW devices was calculated using Equation (11) and at the point (0,0) which is in the middle of the SAW device where the chamber is placed at.

Figure 2 shows the simulation and experimental results of microparticle patterning when the device was applied with its A0 mode (frequency of 13 MHz) to form SSAWs (the frequency details are given in Table 1) from cross-sectional and top views. The curvature (K) value was changed from 0 (flat) to ±60 m^{-1}, ±200 m^{-1} and then ±600 m^{-1} for simulations and experiments.

Figures 2(a-1) and 2(a-2) show the cross-sectional views of simulation results for acoustic pressure field and particle patterning (after applied with SAW for 10 seconds) on the flat geometry (e.g., the conventional SSAWs case). In this case, the microparticles are aligned onto the pressure nodes of the acoustic pressure field, in parallel lines with a nearly constant line distance.

Figures 2(b) to 2(d) present the simulation and experimental results of particle patterning on concave geometries of the flexible SAW device. Numbers (1) to (4) in the figures show the acoustic pressure field (Pa) simulation, particle alignment from the cross-sectional view after simulation for 10 seconds, experimental results for particle alignment from cross-sectional view and top view, respectively. For the concave geometries, the patterned lines of particles become converged and have shown a slope towards the centre of the curvature of the device (see Figures 2(b) to 2(d), with different bending curvatures). For the concave geometries of the SAW device, when the centre of curvature of the device is located inside the chamber (Figure 2(b)), the particle lines will be converged towards the centre of curvature of the device but then diverged after passing through the centre of curvature. The line distances start to decrease as the lines are converged towards the centre of curvature, and after passing that point the lines start to diverge and the line distances start to increase.

With the increase of curvatures of the concave geometries, there appears a weak acoustic pressure region (acoustic pressure is near zero, e.g., dotted black circle in Figure 2(d-1)), however, there are still pressure nodes (zero pressure positions) present in this area and the particles will pattern on the pressure nodes. But since this is a weak pressure region, the particles will not be patterned in complete lines and some still remain in the space between pressure nodes. We can see the accumulation of particle lines in this area. Additionally, Figure

2(d-2) shows that the particles at the two sides of the microchamber do not form any pattern which is attributed to the weak SSAW field at these positions with apparently random distribution of particles. Most particles aggregate at the two sides as shown in Figure 2(d-2) which have small pressure node regions (see the areas marked with dotted blue circles in Figure 2(d-2)). On the concave geometries, we can see clear particle patterning where the SSAW field is focused in the middle (e.g. the area marked with dotted blue circle in Figure 2(c-2)).

The simulation and experimental results of particle patterning on convex geometries of the flexible SAW device are shown in Figures 2(e) to 2(g). It should be noted that numbers (1) to (4) define the acoustic pressure field (Pa) simulation, particle alignment from the cross-sectional view after simulation for 10 seconds, experimental results for particle alignment from cross-sectional view and top view, respectively. For the convex geometries, the particle lines have the opposite trends (i.e. compared with those of concave ones). They become diverged and have a slope away from centre of the curvature of the device as shown in Figures 2(e) to 2(g) at different bending curvatures. The line distances are increased as the lines are diverged away from the centre of curvature. Increasing the bending curvature of the convex devices results in a weaker SSAW field especially near the top of the chamber (e.g., the area marked with dotted blue circles in Figure 2(g-2)) and the particles are randomly distributed in these areas. Further increase in the curvature causes the SSAW field to become even weaker and the particles will be randomly distributed inside the chamber. For these convex geometries, the patterning is clearer near the surface of the SSAW device compared to that on the top of the chamber (e.g. Figure 2(g-2)).

The experimental results for cross-sectional views (which are located at the bottom of the microchamber) are consistent with the simulation results. We also compared the slopes of the particle lines for both the concave and convex geometries from the cross-sectional views in order to show the convergence and the divergence of the lines (The results are presented in Figure S-3 in the supplementary information). The top views presented in Figure 2 show that particles are aligned in parallel corresponding to the pressure nodes of the acoustic pressure field of the SSAWs. For both the concave and convex geometries, the line distances are not constant unlike the particle patterning on the flat SSAW devices. For the concave curvature of $K = 600$ m^{-1} (Figure 4(d-4)), particle patterning seems to be irregular. We believe that this is caused by the large acoustic pressure node area in the middle of the chamber (as has been confirmed from simulation results, e.g., the green area shown in Figure 2(d-1)), as the particles tend to move towards the pressure node area, and the patterns become irregular.

Particle patterning was further performed on the concave geometries of Device 1 using the higher resonant frequencies of S0 and A1 modes (details are given in Table 1). The obtained results all show the patterning of particles using the SSAWs. With the increase of frequencies, the distributions of lines are similar as those under the A0 mode, but the line distances become smaller.

(a-1) **(a-2)**

−4.0e⁵ 0 4.0e⁵ [Pa]

(b-1) **(b-2)** **(b-3)** **(b-4)**

−4.0e⁵ 0 4.0e⁵ [Pa]

(c-1) **(c-2)** **(c-3)** **(c-4)**

−4.5e⁵ 0 4.5e⁵ [Pa]

(d-1) **(d-2)** **(d-3)** **(d-4)**

−4.5e⁵ 0 4.5e⁵ [Pa]

(e-1) **(e-2)** **(e-3)** **(e-4)**

−3.5e⁵ 0 3.5e⁵ [Pa]

(f-1) **(f-2)** **(g-1)** **(g-2)**

— **200 μm** — **200 μm** — **200 μm** — **200 μm**

-3.5e⁵ 0 3.5e⁵ [Pa]   -3.5e⁵ 0 3.5e⁵ [Pa]
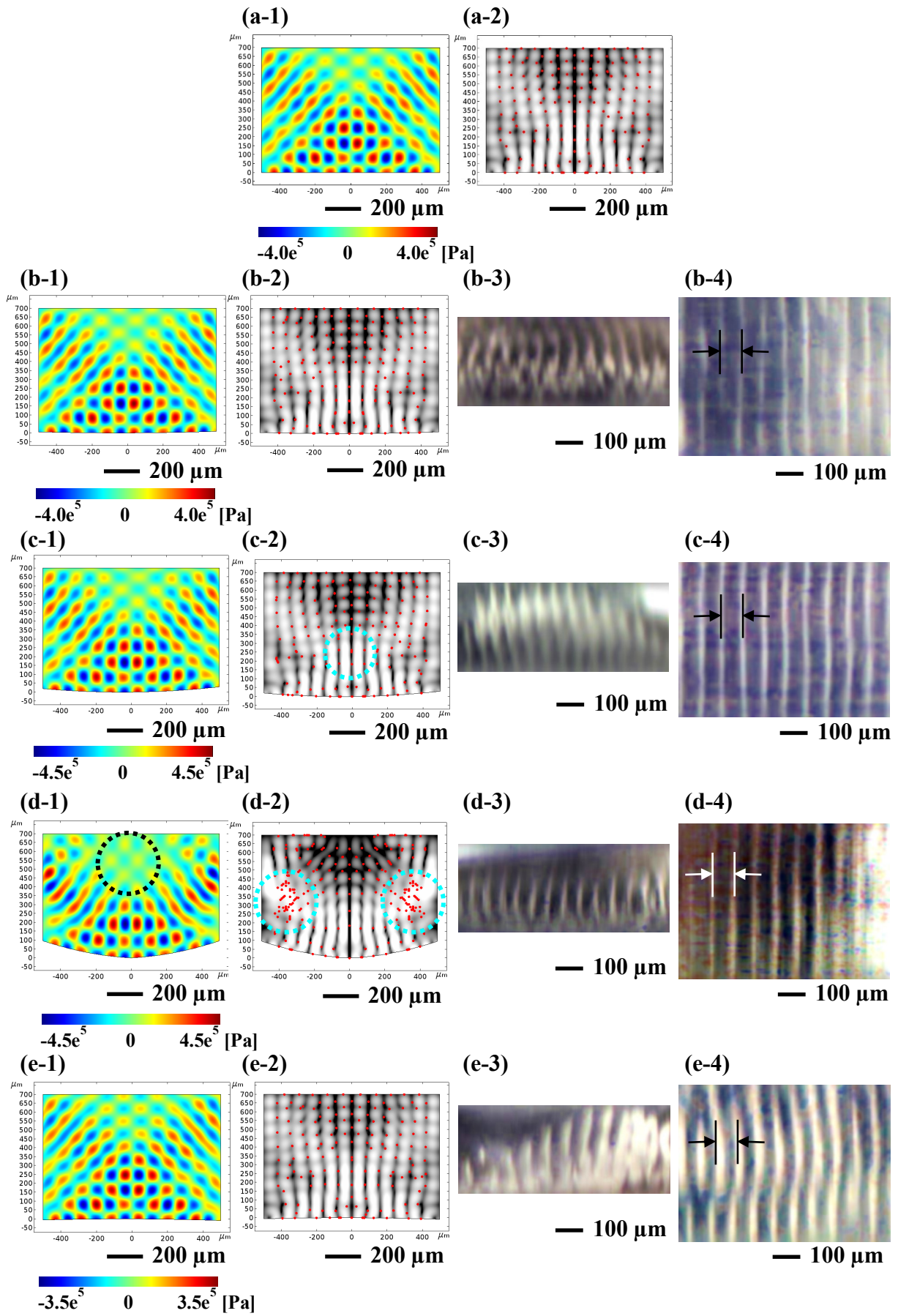
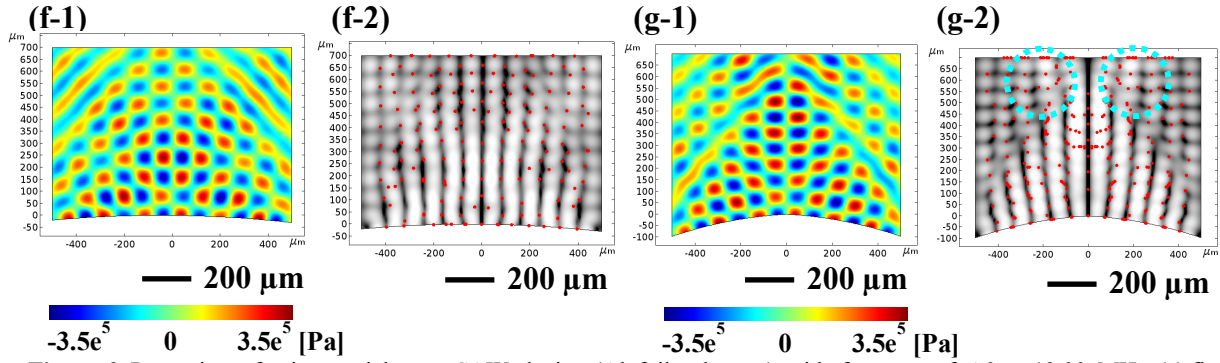**Figure 2** Patterning of microparticles on SAW device (Al foil substrate) with frequency f_A0 = 13.00 MHz (a) flat, (b) concave Ҝ = 60 m⁻¹, (c) concave Ҝ = 200 m⁻¹, (d) concave Ҝ = 600 m⁻¹, (e) convex Ҝ = -60 m⁻¹, (f) convex Ҝ = -200 m⁻¹, (g) convex Ҝ = -600 m⁻¹, simulation of (1) acoustic pressure (Pa), (2) particle alignment from cross-sectional view after 10 s and experimental particle alignment from (3) cross-sectional and (4) top views.

Based on the results shown in Figure 2, the line distances are dramatically different from the top view and cross-section views. Figures 3(a) to 3(d) summarise the simulation data of line distances through the width of the microchamber at the top (Figures 3(a) and 3(b)) and also at half way up from the surface of the SAW device (Figures 3(c) and 3(d)) for both the concave and convex geometries.

For the concave geometries, at the top of the chamber, the line distances at the two sides of the microchamber are smaller than those in the middle of the chamber (Figure 3(a)). However, at half way up from the surface of the SSAW device, the results are quite different depending on the curvature and geometry of the SSAW device (Figure 3(b)). For the two smaller concave curvatures (60 m⁻¹ and 200 m⁻¹), there is a similar trend compared with the line distances at the top of the chamber, but there is a decrease in the line distance values in the centre of the chamber. Whereas for the two larger concave curvatures (600 m⁻¹ and 2000 m⁻¹), the distribution trends of line distances are the opposite to that at the top of the chamber i.e. the line distances at the sides of the chamber are slightly larger than those in the middle of the chamber.

For the convex geometries, the trends for the line distances at the top of the chamber are dependant on curvature and geometries of the SSAW device (Figure 3(c)). For the smallest convex curvature (-60 m⁻¹), the trends for the line distances are nearly the same as the flat device. For the convex curvature of 200 m⁻¹, the line distances at the two sides of the microchamber are smaller than those in the middle of the chamber. But for the 400 m⁻¹ convex curvature, there is a slight decrease of the line distance values in the middle of the chamber. Whereas at the half way up from the surface of the SAW device, the trends for the line distances at the top of the chamber are reversed compared to the concave geometries (at the top of the chamber) i.e., the line distances at the sides of the microchamber are slightly larger than those in the middle of the microchamber (Figure 3(d)).

Figures 3(e) and 3(f) compares the line distances of the experimental data from the top views through the width of the chamber for concave and convex geometries, respectively. The line distances are nearly constants for the flat device. For the concave geometries, the line distances at the two sides of the microchamber are smaller than those in the middle. Whereas for the convex geometry, the trends are reversed, i.e., the line distances at the sides of the microchamber are larger than those in the middle of the chamber. The experimental results show the same trends as those from the simulation results shown in Figures 3(a) to 3(d). Since in the experimental cases the SAW devices are not bent into perfectly symmetric curves, there are slight asymmetry of data in the experimental graphs.

In brief, our simulation results shown in Figure 3 clearly show the patterns of the particle distributions for both the concave and convex bending situations. For the concave geometries of the SAW device, the acoustic field would be focused, whereas for the convex geometries, the acoustic field would be diverged. These phenomena are similar to the results reported by Lim et al [51], who found that a non-flexible and spherical PZT with outer and inner surfaces representing convex and concave geometries could generate similar phenomena.
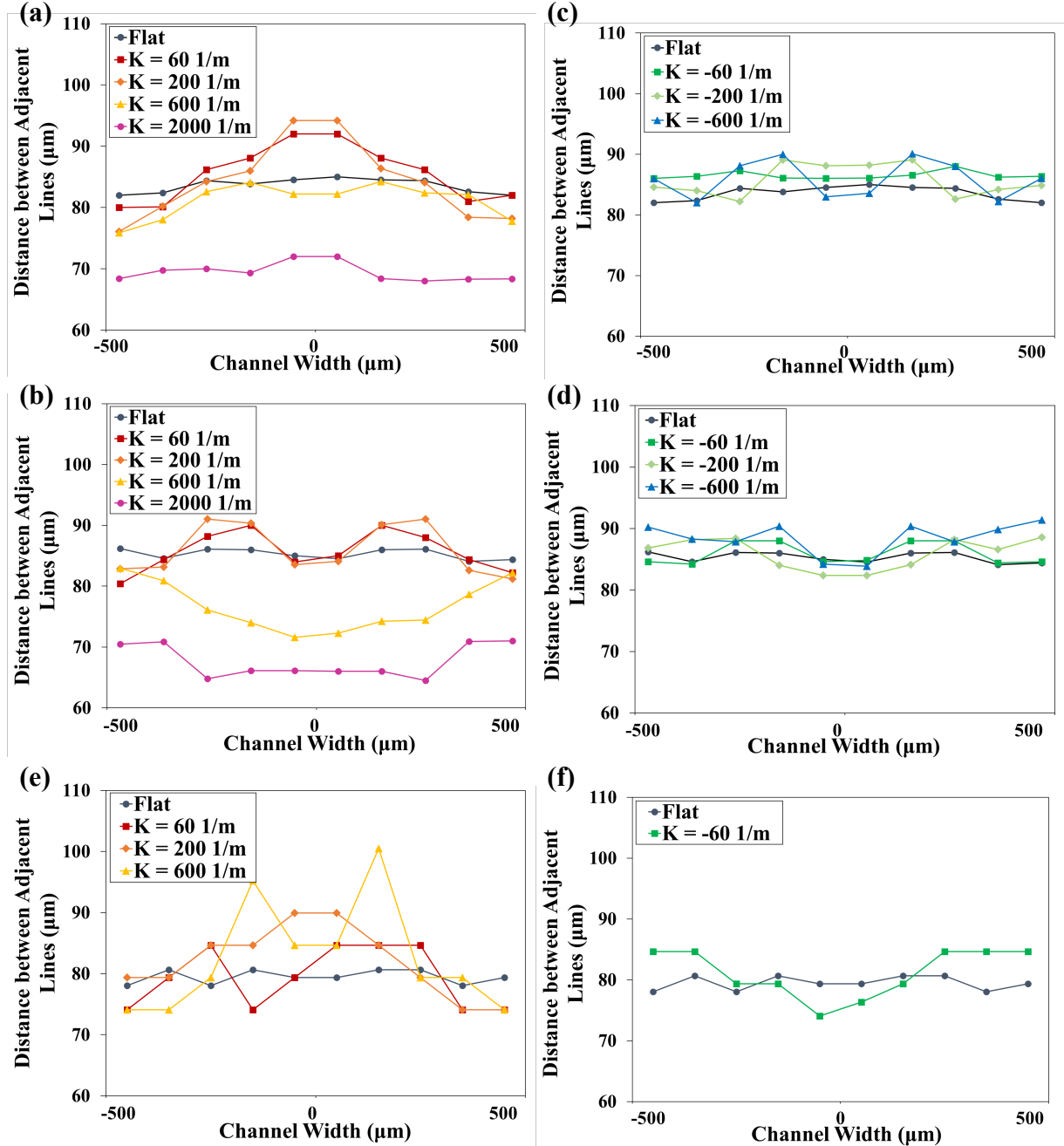

Figure 3 Comparison of the line distances with frequency of f_{A0} = 13.00 MHz (a) at the top of the chambe0; (b) half way up from the surface of the SAW device for concave geometries; (c) the top of the chamber; (d) half way up from the surface of the SAW device for convex geometries, all simulation results from cross-sectional view; (e) concave; (f) convex geometries, experimental data from top view.

4.2 Lamb Wave Based SSAW on Al Sheet with 400 μm Wavelength

For the second group of experimental studies, we have chosen Device 2 (with Al sheet thickness of ~ 200 μm and a wavelength of 400 μm and its details are given in Table 1). This

11

is a bendable device but with less flexibility because of its thickness. The surface finishing is slightly rougher than that of the Al foil in the previous case. In this case, we will focus more on the significantly bent Al sheet devices with very large curvatures (e.g., 1125 m^{-1} and 2564 m^{-1}) as for this thickness of Al sheet it can be stably fixed at its bent shape. This device exhibits three modes of A0, S0 and S1 Lamb waves as shown in Figure S-1(b).

Figure 4 shows the simulation and experimental results for the acoustic pressure and particle patterning from cross-sectional and top views on concave devices agitated using A0 mode with two cases of curvatures of (1125 m^{-1} and 2564 m^{-1}).

Figures 4(a-1) and 4(b-1) show the simulation results of the acoustic pressure field and the pressure nodes. Figures 4(a-2) and 4(b-2) present the simulation results for particle patterning on the concave SAW device. Based on these simulation results of significantly bent conditions, the particle lines first converge towards the centre of curvature, then diverge after passing through the centre of curvature. When the concave curvature is 1125 m^{-1}, the centre of curvature is within the chamber (Figure 4(a-1)). However, when the concave curvature is increased to 2564 m^{-1}, the centre of curvature will appear below the chamber (Figure 4(b-1)). As previously discussed, at such extremely deformed geometries, there are weak acoustic fields at edges (as shown in Figures 4(a-1) and 4(b-1)). The larger the curvature, the more randomly distributed acoustic wave fields with enlarged areas at two sides of the chamber can be observed (Figure 4(b-1)). Because of this reason, strong streaming patterns will appear on both sides of the chamber (which have been confirmed from the experimental observations). This will lead to irregular particle arrangements at those positions (marked with dotted blue circles as shown in Figure 4(a-2) and 4(b-2)). Figures 4(a-3) and 4(b-3) show the corresponding experimental results from cross-sectional views of particle patterning. The particle lines for both concave conditions have been converged towards their centres (the images are locations near the bottom of the chamber) and the experimental and simulation results are consistent with each other.

We have further simulated the bent SAW device with a curvature of 6500 m^{-1}, and the cross-sectional views of particle alignments and pressure distribution are shown in Figures 5(c-2) and 5(c-3). Figures 5(c-2) shows that the particle alignment became irregular and significantly distorted. At the surface of the SAW device, the vertical spacing of lines have been increased, which is even larger than the horizontal distance. This is opposite to the flat SAW device case shown in Figures 5(a-1) and 5(b-1). Also, the simulation shows that at the surface of the bent SAW device, the particles are aligned converging to the centre of the curvature. Whereas the particles located at the top of the chamber are aligned diverging away from centre of the curvature. Therefore, this will cause chaotic distribution of particles from both top and cross-sectional views. This is probably the reason that we did not observe any well-patterned alignment from either top or cross-sectional views experimentally.

Figures 5(a-4) and 5(b-4) show two selected top view images of particle patterns on different concave and convex geometries using the A0 mode (the resonant frequency details are given in Table 1). All the other images for different bending curvature cases are shown in the supplementary information (Figure S-4). In these figures, on the convex geometries, the line distances are larger than those at the same distance in the chamber on concave geometries. In all the conditions, the line distances on both sides of the chamber are slightly larger than the line distances in the centre. As the frequency increases, the line distances decrease.

Figures 4(a-5) and 4(b-5) show the line distances at different heights (bottom, middle, top) of the chamber, obtained from simulation results. In all conditions, the line distances at two sides

of the chamber are slightly larger than those at the centre. It can be seen from Figure 4(a-5), the line distances at the bottom of the chamber are larger than the distances at the middle, because the particle lines have been converged in this area. Near the top of the chamber, the particle lines begin to diverge, so the line distances at the top of the chamber is also larger than the line distances at the middle. When the concave curvature is large (Figure 4(b-5)), the centre of curvature appears below the chamber, so the particle lines inside the chamber are all divergent. As shown in Figure 4(b-5), the closer to the top of the chamber, the larger the line distances.

The line distances at bottom of the chamber in the experiment can be obtained from Figures 4(a-3) and 4(b-3), and the distances at top of the chamber can be obtained from Figures 4(a-4) and 4(b-4). The results are shown in Figures 4(a-6) and 4(b-6). In all conditions, the line distances at two sides of the chamber are larger than those at the centre. It can be seen from Figure 4(a-6), the line distances at the bottom of chamber are similar to the distances at the top for the concave device with the smaller curvature of 1125 m^{-1}. However, for the larger curvature of 2564 m^{-1} the line distances at the bottom of chamber are smaller than the distances at the top in Figure 4(b-6). This shows that increasing the curvature of the flexible devices increases the convergence of the particle pattern lines. The experimental results are in good agreement with the simulation results. In the experiments, the SAW devices are not bent into perfectly symmetric curves. The asymmetry of these SAW device curves results in slight asymmetry of data in the experimental graphs.
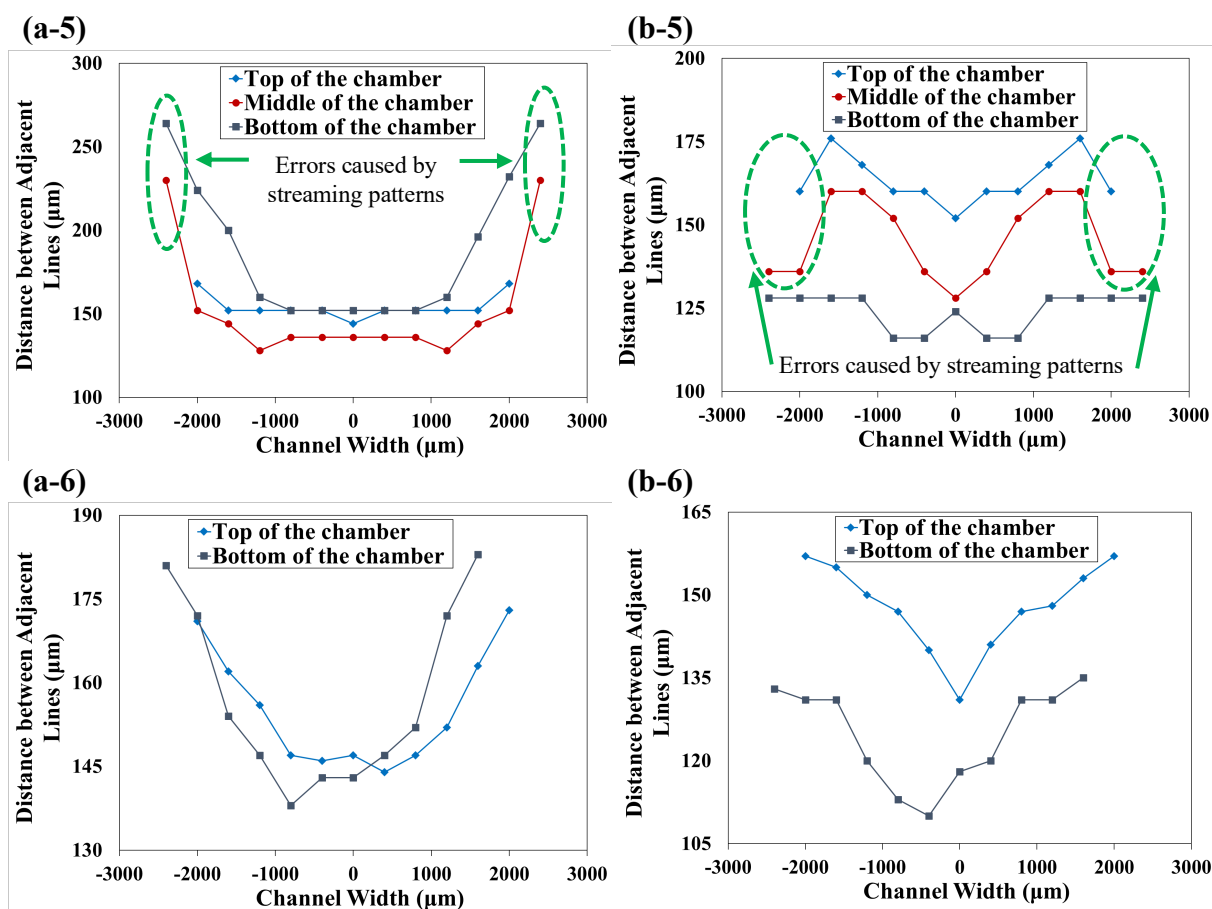

13
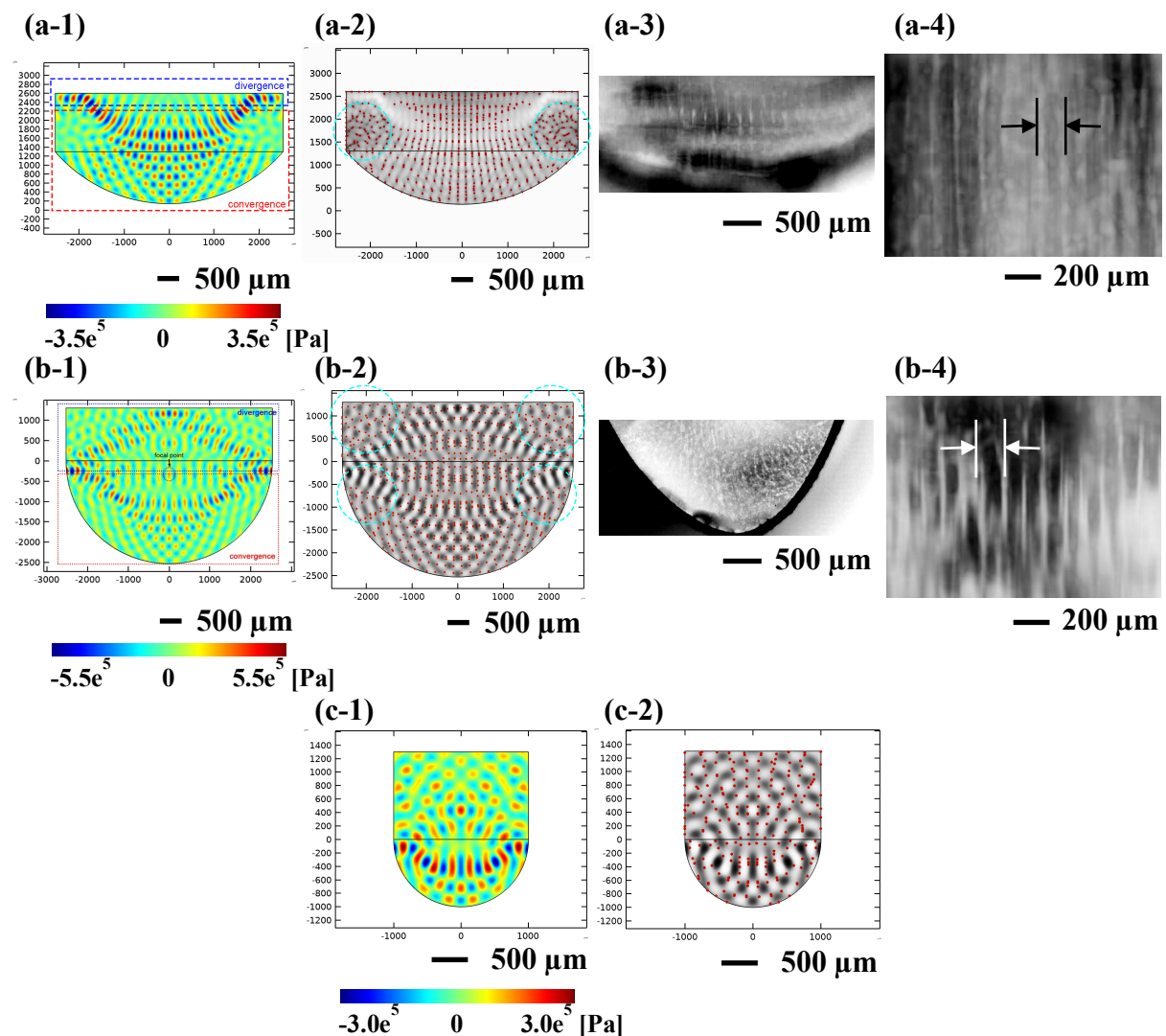
Figure 4 Patterning of microparticles on SAW device (Al plate substrate) with frequency of f_A0 = 6.03 MHz (a) concave Ƙ = 1125 m⁻¹, (b) concave Ƙ = 2564 m⁻¹, (c) concave Ƙ = 6500 m⁻¹; simulation of (1) acoustic pressure (Pa); (2) particle alignment after 10 s and experimental results form (3) cross-sectional; (4) top views and comparison of the line distances from cross-sectional view at different heights from (5) simulation; (6) experiment.

4.3 Rayleigh Wave Device

In the third experimental case, effects of bending curvatures of Device 3 with a substrate thickness of 200 μm and a wavelength of 160 μm (details given in Table 1) were studied. In this device, Rayleigh mode was dominant (frequency of 17 MHz), and was utilized for generating standing waves (as the wavelength is smaller than the substrate thickness, and more information on Rayleigh wave can be found in the supplementary information). The simulation and experimental results of patterning of silica microparticles from the cross-sectional and top views and the graphs comparing the line distances are shown in Figures S-5 and S-6, respectively, in the supplementary information.

The patterning of microparticles is consistent with those obtained from the Lamb wave device. However, for the Rayleigh wave device, the particle patterns are not well defined when using the Rayleigh wave mode, which might be due to the large values of roughness of the surface of the aluminium plate used in fabricating the SSAW devices. Compared with those of Lamb waves which are propagating mostly along the whole plates, the Rayleigh waves propagate much nearer to the surface of the device, thus the surface roughness will have more significant influence for the distortion of the patterns of particles.

14

Simulations were performed for the particle patterning and modelling of acoustic pressure fields on different concave and convex geometries from the cross-sectional views based on the parameters of the Rayleigh mode waves. The simulation results agree well with the experimental data, both of which show the convergence and divergence of the particle lines for concave and convex geometries.

With the increase of the concave bending curvature, a large acoustic pressure node area, formed near the top of the chamber which will cause all the particles in this area to accumulate into two lines in the middle of the chamber. Whereas at the two sides of the chamber, there is a weak SSAW field formed, thus there are accumulated particles and poor alignment patterns at these locations. With the increase of the convex bending curvature up to 200 m^{-1}, the particle patterning is clear and regular. However further increase of the bending curvature causes the deterioration of alignment patterns for microparticles.

For the concave geometries of the SAW Device 3, the particles are patterned well in line positions in the middle of the chamber. However, for the convex geometries, it is harder to obtain a larger area with regular patterns on all the curvatures (apart from the curvature of -200 m^{-1}), probably because of the weaker acoustic SSAW pressure field. From both experimental and simulation results, we can conclude that for this Rayleigh wave device, the concave bending geometries result in more regular particle patterns.

We further compared particle patterning obtained from the Rayleigh wave device with the Lamb wave device results. For the concave geometries with the same curvatures 200 m^{-1}, the Lamb wave device produces regular particle patterns near the lower half of the chamber, but the patterns of the particles are similar at upper heights of the chamber for both devices. Whereas for the convex geometry with the same curvature -200 m^{-1}, particles are patterned more regularly for the Rayleigh wave device through the height of the chamber, if compared with those from the Lamb wave device. For the Lamb wave device, the patterning is regular at the lower half of the chamber compared to the upper half. The reason for this phenomenon can be explained by the fact that the Rayleigh waves (which propagate nearer to the device's surface) could have interacted effectively with the liquid, and thus be dissipated more efficiently into the liquid. This will result in regular patterns of particles in the vertical direction and 3D pattern. Lamb wave (A0 mode) is the flexural wave, which is less efficient to transfer the energy into the liquid.

4.4   Patterning Demonstration Using Twisted ZnO/Al Foil Device

In addition to being bent into various concave and convex surfaces, our flexible SAW devices can also be twisted in different geometries (e.g., with one illustration in Figure 1(d)). Twisting the SAW device actually changes the IDTs' positions from two parallel ones into two IDTs with an inclined direction and a twisting angle (compared with the similarly positioned chamber walls), but also each of the IDTs has been bent into a shape with a curvature (see Fig. 1(d)). We further investigated the effects of different twisting-up geometries of the flexible SAW Device 1 on particle patterning. Different twisting geometries of the flexible SAW devices are shown in the supplementary information (Figure S-7).

Figures 5(a) and 5(b) show two selected top view images of microparticle patterning when the flexible Device 1 was twisted up along 45 degree from the original IDT directions, with twisting angles of (a) 115° and (b) 95°. They were all applied with the A0 mode to form SSAWs (the frequency details are given in Table 1). The IDT directions in these two cases are indicated as shown in Figure 6(a) and 6(b).

The microparticles were found to be patterned into regularly distributed lines which are parallel to the deformed IDTs of the SAW device for all the different twisting geometries. It can also be observed that with the increase of twisting-up curvatures, the lines are inclined but still in parallel to the IDTs, although there are imperfect lines formed, probably due to the significantly bent and inclined two IDTs (see Figure 6(b)). We also observed that the width of each line is quite broad, due to the deformed and bent IDTs.
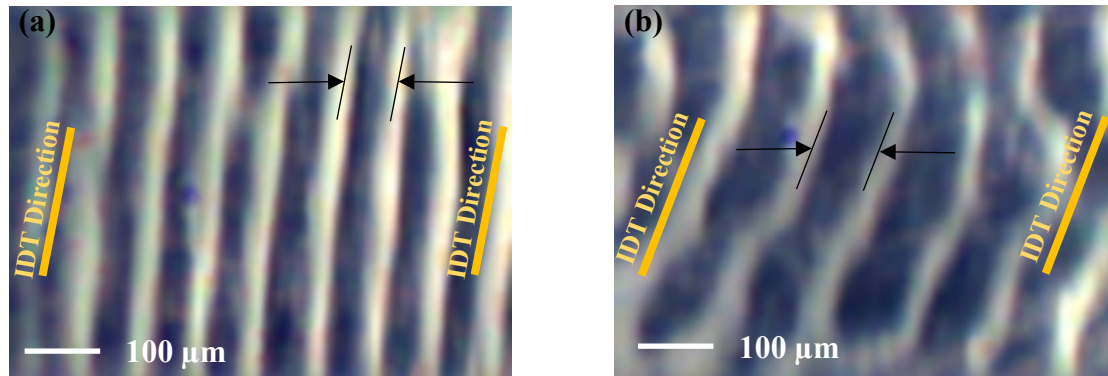

Figure 5 Patterning of silica microparticle patterning on twisted ZnO thin film on Al foil substrate flexible SAW device with frequency f_A0 = 13.00 MHz and (a) twisting angle 115°, (b) twisting angle 95° and for a microchamber parallel to the IDTs from the top view.

4.5 Demonstration Using Yeast Cell Patterning

Yeast cells were patterned on different concave geometries using both the Devices 1 and 3, and the top and cross-sectional views of examples for the cell patterning are shown in Figure S-8 in supplementary information. Similar to those of the microparticles, these yeast cells can be patterned at the pressure nodes of the acoustic pressure field in lines which are convergent as clearly seen from the cross-sectional views. We showed that using our flexible SAW devices, it is possible to manipulate and pattern biological cells despite their large size variations and their strong tendency to adhere to each other. In literature, a lot of studies [8-12] have shown that SAW manipulation is biocompatible, which will conserve cell viability and proliferation with minimal or insignificant change of the cells functionality. It was reported that after SAW manipulation the cells remained alive and were able to reproduce and function normally even after a day [8, 9]. SAW manipulation was proved to cause no significant damage to the cell's physiology [10]. It was shown that if low voltages are used for SAW manipulation, there are minimal effects on the cell's viability. However increased voltages should be used with caution as it may affect cells' viability adversely [11, 12]. So it will be possible to design and build different flexible acoustofluidic systems such as flexible acoustic cell tweezers, flexible acoustic microparticle/cell sorters and even flexible enrichment setups using our flexible/bendable SAW devices.

5 Conclusions

In this paper, we investigated the acoustofluidic behaviour of flexible SAW devices using Rayleigh and Lamb wave modes and studied the effects of different bending curvatures and twisting geometries of these flexible SAW devices on patterning of microparticles and cells in a microchamber which demonstrates the possibility of applying our flexible acoustofluidic systems into biological applications.

- Bending the flexible SAW devices in concave geometries results in the particle pattern lines to become converged with a slope towards the centre of the curvature of the geometry.

Significantly increasing the curvature of the concave geometries will result in the alignment of particles approximately parallel in the middle of the chamber. However, weak particle patterning is also observed at the two sides of the microchamber due to the weaker SSAW field in these areas.

- Bending the flexible SAW devices in convex geometries changes the distribution of particle pattern lines; they become diverged with a slope away from centre of the curvature of the geometry. For the convex geometries, increasing the curvature of the devices will cause a stronger pressure anti-node area near the middle of the microchamber which will drive the particles away from these areas. With further increase in the curvature of the convex geometries, a weaker SSAW field acoustic pressure node area forms in the middle of the chamber near the top, and the particles accumulate there with a poor pattern.

- For the concave geometry, particle alignment is more efficient near the surface of the Lamb wave device. Whereas for the same convex geometry, for the Rayleigh wave device the patterning is more efficient at the top of the chamber, mainly because of the efficiency of wave energy dissipation into the liquid to form SSAWs.

- Particle patterning was performed on twisted SAW devices which resulted in changes to the IDTs positions' from original flat and parallel ones to those with an inclined direction at a twisting angle. In these cases, the microparticles patterned into lines parallel to the twisted IDTs for each twisting geometry.

6 Acknowledgments

7 References

[1] J. Friend and L. Y. Yeo, "Microscale Acoustofluidics: Microfluidics Driven via Acoustics and Ultrasonics," *Reviews of Modern Physics,* vol. 83, no. 2, pp. 647-704, 06/20/ 2011, doi: 10.1103/RevModPhys.83.647.

[2] P. Li and T. J. Huang, "Applications of Acoustofluidics in Bioanalytical Chemistry," *Analytical chemistry,* vol. 91, no. 1, pp. 757-767, 2018, doi: 10.1021/acs.analchem.8b03786.

[3] T. J. Huang, "Acoustofluidics: Merging Acoustics and Microfluidics for Biomedical Applications," *The Journal of the Acoustical Society of America,* vol. 145, no. 3, pp. 1786-1786, 2019/03/01 2019, doi: 10.1121/1.5101531.

[4] G. M. Whitesides, "The Origins and the Future of Microfluidics," *Nature,* vol. 442, p. 368, 2006, doi: 10.1038/nature05058.

[5] X. Ding *et al.*, "Surface Acoustic Wave Microfluidics," *Lab on a chip,* 10.1039/C3LC50361E vol. 13, no. 18, pp. 3626-3649, 2013, doi: 10.1039/C3LC50361E.

[6] Y. Q. Fu *et al.*, "Advances in Piezoelectric Thin Films for Acoustic Biosensors, Acoustofluidics and Lab-on-Chip Applications," *Progress in Materials Science,* vol. 89, pp. 31-91, 2017, doi: 10.1016/j.pmatsci.2017.04.006.

[7] W. Connacher *et al.*, "Micro/Nano Acoustofluidics: Materials, Phenomena, Design, Devices and Applications," *Lab on a chip,* vol. 18, no. 14, pp. 1952-1996, 2018.

[8] K. Wang *et al.*, "Sorting of Tumour Cells in a Microfluidic Device by Multi-Stage Surface Acoustic Waves," *Sensors and Actuators B Chemical,* vol. 258, 2017, doi: 10.1016/j.snb.2017.12.013.

[9] M. Wu *et al.*, "High-Throughput Cell Focusing and Separation via Acoustofluidic Tweezers," *Lab on a chip,* vol. 18, no. 19, pp. 3003-3010, 2018.

[10] X. Ding *et al.*, "Cell Separation Using Tilted-Angle Standing Surface Acoustic Waves," *Proceedings of the National Academy of Sciences,* vol. 111, no. 36, pp. 12992-12997, 2014.

[11] K. Mutafopulos *et al.*, "Traveling Surface Acoustic Wave (TSAW) Microfluidic Fluorescence Activated Cell Sorter (µFACS)," *Lab on a chip,* vol. 19, no. 14, pp. 2435-2443, 2019.

[12] J. Nam, H. Lim, C. Kim, J. Yoon Kang, and S. Shin, "Density-Dependent Separation of Encapsulated Cells in a Microfluidic Channel by Using a Standing Surface Acoustic Wave," (in eng), *Biomicrofluidics,* vol. 6, no. 2, pp. 24120-2412010, Jun 2012, doi: 10.1063/1.4718719.

[13] S. Liu *et al.*, "Investigation into the Effect of Acoustic Radiation Force and Acoustic Streaming on Particle Patterning in Acoustic Standing Wave Fields," *Sensors (Basel, Switzerland),* vol. 17, no. 7, p. 1664, 2017, doi: 10.3390/s17071664.

[14] G. Destgeer and H. J. Sung, "Recent Advances in Microfluidic Actuation and Micro-Object Manipulation via Surface Acoustic Waves," *Lab on a chip,* vol. 15, no. 13, pp. 2722-2738, 2015.

[15] T. D. Nguyen, V. T. Tran, Y. Q. Fu, and H. Du, "Patterning and Manipulating Microparticles into a Three-Dimensional Matrix Using Standing Surface Acoustic Waves," *Applied Physics Letters,* vol. 112, no. 21, p. 213507, 2018.

[16] X. Tao *et al.*, "3D Patterning/Manipulating Microparticles and Yeast Cells Using ZnO/Si Thin Film Surface Acoustic Waves," *Sensors and Actuators B: Chemical,* vol. 299, p. 126991, 2019.

[17] Z. Tian *et al.*, "Wave Number–Spiral Acoustic Tweezers for Dynamic and Reconfigurable Manipulation of Particles and Cells," *Science advances,* vol. 5, no. 5, p. eaau6062, 2019.

[18] N.-T. Nguyen, "Research Highlight Soft Microsystems - A Paradigm Shift in Engineering Small Systems," *Micro and Nanosystems,* vol. 7, pp. 2-3, 07/29 2015, doi: 10.2174/187640290701150729123546.

[19] R. Tao *et al.*, "Thin Film Flexible/Bendable Acoustic Wave Devices: Evolution, Hybridization and Decoupling of Multiple Acoustic Wave Modes," *Surface and Coatings Technology,* vol. 357, pp. 587-594, 2019.

[20] D. P. Holmes, B. Tavakol, G. Froehlicher, and H. A. Stone, "Control and Manipulation of Microfluidic Flow via Elastic Deformations," *Soft Matter,* vol. 9, no. 29, pp. 7049-7053, 2013.

[21] Z. Yang, Y. Zhang, T. Itoh, and R. Maeda, "A Novel MEMS Compatible Lab-on-a-Tube Technology," *Lab on a chip,* vol. 14, no. 24, pp. 4604-4608, 2014.

[22] K. Sato, S. Kamada, and K. Minami, "Development of Microstretching Device to Evaluate Cell Membrane Strain Field Around Sensing Point of Mechanical Stimuli," *International Journal of Mechanical Sciences,* vol. 52, no. 2, pp. 251-256, 2010.

[23] J. Kim, J. B. You, S. M. Nam, S. Seo, S. G. Im, and W. Lee, "Rollable Microfluidic Systems with Microscale Bending Radius and Tuning of Device Function with Reconfigurable 3D Channel Geometry," *ACS applied materials & interfaces,* vol. 9, no. 12, pp. 11156-11166, 2017.

[24] S. Wang, T. Chinnasamy, M. A. Lifson, F. Inci, and U. Demirci, "Flexible substrate-based devices for point-of-care diagnostics," *Trends in biotechnology,* vol. 34, no. 11, pp. 909-921, 2016.

[25] M. Focke, D. Kosse, C. Müller, H. Reinecke, R. Zengerle, and F. von Stetten, "Lab-on-a-Foil: Microfluidics on Thin and Flexible Films," *Lab on a chip,* vol. 10, no. 11, pp. 1365-1386, 2010.

[26] Y. Yang, S. Xing, Z. Fang, R. Li, H. Koo, and T. Pan, "Wearable Microfluidics: Fabric-Based Digital Droplet Flowmetry for Perspiration Analysis," *Lab on a chip,* vol. 17, no. 5, pp. 926-935, 2017.

[27] S. Y. Lee *et al.*, "Water-Resistant Flexible GaN LED on a Liquid Crystal Polymer Substrate for Implantable Biomedical Applications," *Nano Energy,* vol. 1, no. 1, pp. 145-151, 2012.

[28] G. T. Hwang, M. Byun, C. K. Jeong, and K. J. Lee, "Flexible Piezoelectric Thin‐Film Energy Harvesters and Nanosensors for Biomedical Applications," *Advanced healthcare materials,* vol. 4, no. 5, pp. 646-658, 2015.

[29] S. R. Krishnan *et al.*, "Epidermal Electronics for Noninvasive, Wireless, Quantitative Assessment of Ventricular Shunt Function in Patients with Hydrocephalus," *Science translational medicine,* vol. 10, no. 465, 2018.

[30] H. Jin *et al.*, "Flexible Surface Acoustic Wave Resonators Built on Disposable Plastic Film for Electronics and Lab-on-a-Chip Applications," *Scientific reports,* vol. 3, p. 2140, 2013.

[31] X. He *et al.*, "High Sensitivity Humidity Sensors Using Flexible Surface Acoustic Wave Devices Made on Nanocrystalline ZnO/Polyimide Substrates," *Journal of Materials Chemistry C,* vol. 1, no. 39, pp. 6210-6215, 2013.

[32] J. Chen *et al.*, "Bendable Transparent ZnO Thin Film Surface Acoustic Wave Strain Sensors on Ultra-Thin Flexible Glass Substrates," *Journal of Materials Chemistry C,* vol. 2, no. 43, pp. 9109-9114, 2014.

[33] R. Tao *et al.*, "Hierarchical Nanotexturing Enables Acoustofluidics on Slippery yet Sticky, Flexible Surfaces," *Nano Letters,* vol. 20, no. 5, pp. 3263-3270, 2020/05/13 2020, doi: 10.1021/acs.nanolett.0c00005.

[34] X. Tao *et al.*, "Three-Dimensional Tetrapodal ZnO Microstructured Network Based Flexible Surface Acoustic Wave Device for Ultraviolet and Respiration Monitoring Applications," *ACS Applied Nano Materials,* vol. 3, no. 2, pp. 1468-1478, 2020.

[35] R. Tao *et al.*, "Bimorph Material/Structure Designs for High Sensitivity Flexible Surface Acoustic Wave Temperature Sensors," *Scientific reports,* vol. 8, no. 1, pp. 1-9, 2018.

[36] Y. Liu *et al.*, "Flexible and Bendable Acoustofluidics Based on Zno Film Coated Aluminium Foil," *Sensors and Actuators B: Chemical,* vol. 221, pp. 230-235, 2015.

[37] Y. Q. Fu *et al.*, "Recent Developments on ZnO Films for Acoustic Wave Based Bio-Sensing and Microfluidic Applications: A Review," *Sensors and Actuators B: Chemical,* vol. 143, no. 2, pp. 606-619, 2010.

[38] D. Botstein and G. R. Fink, "Yeast: An Experimental Organism for 21st Century Biology," *Genetics,* vol. 189, no. 3, pp. 695-704, 2011.

[39] C. T. Crowe, J. D. Schwarzkopf, M. Sommerfeld, and Y. Tsuji, *Multiphase Flows with Droplets and Particles*. CRC press, 2011.

[40] C. T. Crowe, *Multiphase Flow Handbook*. CRC press, 2005.

[41] M. Settnes and H. Bruus, "Forces Acting on a Small Particle in an Acoustical Field in a Viscous Fluid," *Physical Review E,* vol. 85, no. 1, p. 016327, 2012, doi: 10.1103/PhysRevE.85.016327.

[42] L. V. King, "On The Acoustic Radiation Pressure on Spheres," *Proceedings of the Royal Society of London. Series A-Mathematical and Physical Sciences,* vol. 147, no. 861, pp. 212-240, 1934, doi: 10.1098/rspa.1934.0215.

[43] K. Yosioka and Y. Kawasima, "Acoustic Radiation Pressure on a Compressible Sphere," *Acta Acustica united with Acustica,* vol. 5, no. 3, pp. 167-173, 1955.

[44] A. A. Doinikov, "Acoustic Radiation Pressure on a Rigid Sphere in a Viscous Fluid," *Proc. R. Soc. Lond. A,* vol. 447, no. 1931, pp. 447-466, 1994, doi: 10.1098/rspa.1994.0150.

[45] A. A. Doinikov, "Acoustic Radiation Pressure on a Compressible Sphere in a Viscous Fluid," *Journal of Fluid Mechanics,* vol. 267, pp. 1-22, 1994, doi: 10.1017/S0022112094001096.

[46] L. P. Gorkov, "On the Forces Acting on a Small Particle in an Acoustical Field in an Ideal Fluid," *Soviet Physics - Doklady,* vol. 6, pp. 773-775, 1962.

[47] F. Petersson, A. Nilsson, C. Holm, H. Jonsson, and T. Laurell, "Separation of Lipids from Blood Utilizing Ultrasonic Standing Waves in Microfluidic Channels," (in eng), *The Analyst,* vol. 129, no. 10, pp. 938-43, Oct 2004, doi: 10.1039/b409139f.

[48] R. Barnkob, P. Augustsson, T. Laurell, and H. Bruus, "Acoustic Radiation- and Streaming-Iduced Microparticle Velocities Determined by Microparticle Image Velocimetry in an Ultrasound Symmetry Plane," *Physical Review E,* vol. 86, no. 5, p. 056307, 2012, doi: 10.1103/PhysRevE.86.056307.

[49] C. Devendran, T. Albrecht, J. Brenker, T. Alan, and A. Neild, "The Importance of Travelling Wave Components in Standing Surface Acoustic Wave (SSAW) Systems," *Lab on a chip,* vol. 16, no. 19, pp. 3756-3766, 2016, doi: 10.1039/C6LC00798H.

[50] COMSOL, "COMSOL User's Guide", 5.4 ed, 2018.

[51] E. Lim, L. Lee, L. Y. Yeo, Y. M. Hung, and M. K. Tan, "Acoustically Driven Micromixing: Effect of Transducer Geometry," *IEEE transactions on ultrasonics, ferroelectrics, and frequency control,* vol. 66, no. 8, pp. 1387-1394, 2019.